ORIGINAL ARTICLE

Combined methodology for three-dimensional slope stability analysis coupled with time effect: a case study in Germany

Mei Dong[1] · Hui Hu[2] · Jie Song[2]

Abstract

High-steep slopes in open pit mines are much more likely to collapse due to mining operations. Challenges such as data acquisition, precise numerical models and adaptable methodologies have impeded more reliable results of slope stability analysis based on the current methods. Within this context, this paper proposes a combined methodology using light detection and ranging technology to capture high-resolution slope geometry, three-dimensional geological and geotechnical modeling technologies for creating high-quality numerical simulation models and finite-element slope stability analyses combined with a new automatic strength reduction technique to analyze complex geotechnical problems. At the end, the methodology introduces a time series analysis to improve the reliability of the calculated factor of safety. A case study in the deepest open pit mine in Hambach, Germany, was conducted to test and demonstrate the effectiveness and applicability of the proposed methodology.

Keywords Slope stability analysis · 3D geotechnical modeling · Numerical simulation · Automatic strength reduction technology · Light detection and ranging

Introduction

A large number of slope failures have been recorded with respect to human activities, making slope stability analysis a continued and interesting topic in the field of geotechnical engineering (e.g., Kelesoglu 2016; Lin and Chen 2017; Huang et al. 2017). In open pit mines, the most remarkable characteristics are their high and steep slopes, e.g., the Chuquicamata copper mine with a current height of 850 m, the South Africa Palabora copper mine with a current height of 700 m and more. The continuous dynamic influence that mining activities cause creates very dominant slope characteristics in open pit mines. These "ultra-depths" around 1000 m cause a significant level of stress, particularly if the horizontal stresses in situ exceed the vertical stresses. It is therefore important to examine effects of stress on the

stability of high and steep slopes in open pit mines (e.g., Sjoeberg 2000; Arikan et al. 2010; Kaya and Topal 2015).

Presently, the commonly used methods for slope stability analysis are based on limit equilibrium methods (LEMs) (e.g., Bishop 1955; Zhou and Cheng 2013) and numerical simulations (e.g., MacLaughlin and Doolin 2006; Scholtes and Donze 2012; Gonte et al. 2013; Jiang et al. 2015; Ozbay and Gabalar 2015). A potential limitation of LEMs is that certain assumptions must be made relating to the shape or location of the critical failure mechanism, such as the inter-slice force or the stress distribution of the slip surface. Also, they do not account for the stress–strain (deformation force) behavior of the soil (Jiang et al. 2014).

Since numerical methods can take into account both deformations and forces, they can obtain more precise estimates of stress and displacement than LEMs (Nian et al. 2012). With the development of computing systems, numerical simulation techniques have rapidly improved and have been extensively used in recent decades.

Slope status is normally influenced by internal and external factors and other impacts. Internal impacts include the makeup of the rock, clay or sand, the structure of rock or clay (joint or fissure) and ground water (hydrostatic pressure, hydrodynamic pressure, seepage force, uplift pressure and softening impact). External impacts are characterized by anthropogenic

✉ Hui Hu
    Hui.Hu_Ruhr@hotmail.com

[1] Engineering Research Center of Urban Underground Development of Zhejiang Province, College of Civil Engineering and Architecture, Zhejiang University, No. 866 Yuhangtang Road, Hangzhou, People's Republic of China

[2] Hangzhou Ruhr Technology Co., Ltd., No. 8-2 Keji Road, Hangzhou, People's Republic of China

influences (excavation, transportation, blasting) and weathering effects (precipitation, lightening, freeze–thaw, etc.). Other conditions such as slope geometry (convex or concave toward the mining stage) also impact slopes. In addition to the three intrinsic impacts, there are three processes during numerical analysis that can also influence the precision of the results, such as the quality of the geometrical model, the precision of geotechnical parameters and the suitability of the mathematic approach. The challenges for these three processes are described as follows. First, with the development of remote sensing technology, high-resolution digital elevation models (DEMs) of the geometry of the slope can be obtained using a terrestrial laser scanner (TLS). Combining a high-resolution DEM with geotechnical parameters of geological layers for a more reliable numerical model is a challenge, however. Second, due to the complex geological attributes of an exposed slope in an open pit mine, the determination of geotechnical parameters for different geological layers is another challenge. Geotechnical parameters of each soil or rock layer can be determined by laboratory and in situ experiments. However, it is common that the analytic and numerical results of deformation are not compatible with observed values when applying the experimental parameters for analysis. Third, although time-dependent deformation can be measured for time series analysis and deformation prediction, how to implement a time-dependent stability analysis remains a challenge, i.e., designing a mathematical approach to evaluate progressive failure.

In this study, numerical simulation was combined with an automatic strength reduction method to calculate the factor of safety (FOS) of a slope. The engineered slopes in the deepest open pit mine in Hambach, Germany, are used as examples. To improve the precision of the calculated results, 3D structured geological and geotechnical models of the studied slopes were constructed by converting LiDAR scanning data into a numerical model. Finally, a time series safety factor was considered for improving the reliability of the analysis results. The proposed methodology improved the reliability of slope stability analysis in several ways: through LiDAR scanning for high-resolution slope geometry, 3D geological and geotechnical modeling techniques for more precise numerical models and retroactive analysis for more reliable geotechnical parameters. Results from this study have been accepted and adopted by the mining company for improved security measures.

Materials and evaluation of geotechnical parameters

Description of the study site

The Hambach open pit lignite mine is located in the Lower Rhine Embayment in a triangle formed by the cities of

Cologne, Aachen and Dusseldorf of North-Rhine Westphalia, Germany [Fig. 1, Thomas Roemer (OpenStreetMap data)]. The mine is 39.32 km^2 in size (measured in early 2011) and has been approved for expansion up to 85 km^2. It is also the deepest open pit mine in the world with respect to sea level. Scanning operations were carried out to monitor the activity generated by excavation, transportation and other activities in the Hambach mine, as well as to detect any deformation that directly and adversely impacts the current stage of mining. From top to bottom, the mine has undergone seven stages of excavation, and strip mining is now in its seventh stage. Two 3D terrestrial laser scanners (TLS) from Optech and Riegl were deployed during the sixth stage, and the target of the scans was the fifth stage of the slope surface. In order to detect slope deformation, multi-temporal scans were carried out in 2011 on April 1, April 13, May 12 and June 20.

The TLS was deployed on the sixth level of the open pit mine, and the target scanning elevation ranged from − 194 to − 109 m, which is highlighted by two horizontal red lines in Fig. 2 (Schaefer et al. 2005). Figure 2 shows that the scanned slope consisted of two layers, which from upper to lower were made up of a mixed layer of gravel and sand (sand was the dominant material) and a clay layer. The fifth stage of mining was the target of interest and was made up of these two layers.

Mechanism of slope failure of the research area

The common geotechnical problems facing mining slopes are rock burst and collapse in hard rock mines and the time-dependent creep in soft material mines. The research area is characterized by a soil-based slope, so time-dependent creep should be analyzed. For time-dependent deformed slope stability assessment, it is essential to capture and identify the movements within a given time span, which requires sophisticated monitoring technology and analysis. Even though some cases have revealed that slope failure may occur instantaneously due to brittle characteristics, most slope failures take place after accumulating enough displacements. Glastonbury and Fell (2002) interpreted that a combination of developing monitoring systems and warning systems, selecting the appropriate slope deformation criteria and designing stabilization or risk mitigation measures should be the standard method for dealing with slope instability problems.

Pre-evaluation of geotechnical parameters

In practice, many geotechnical parameters are not normally available. In the Hambach open pit mine, parameters
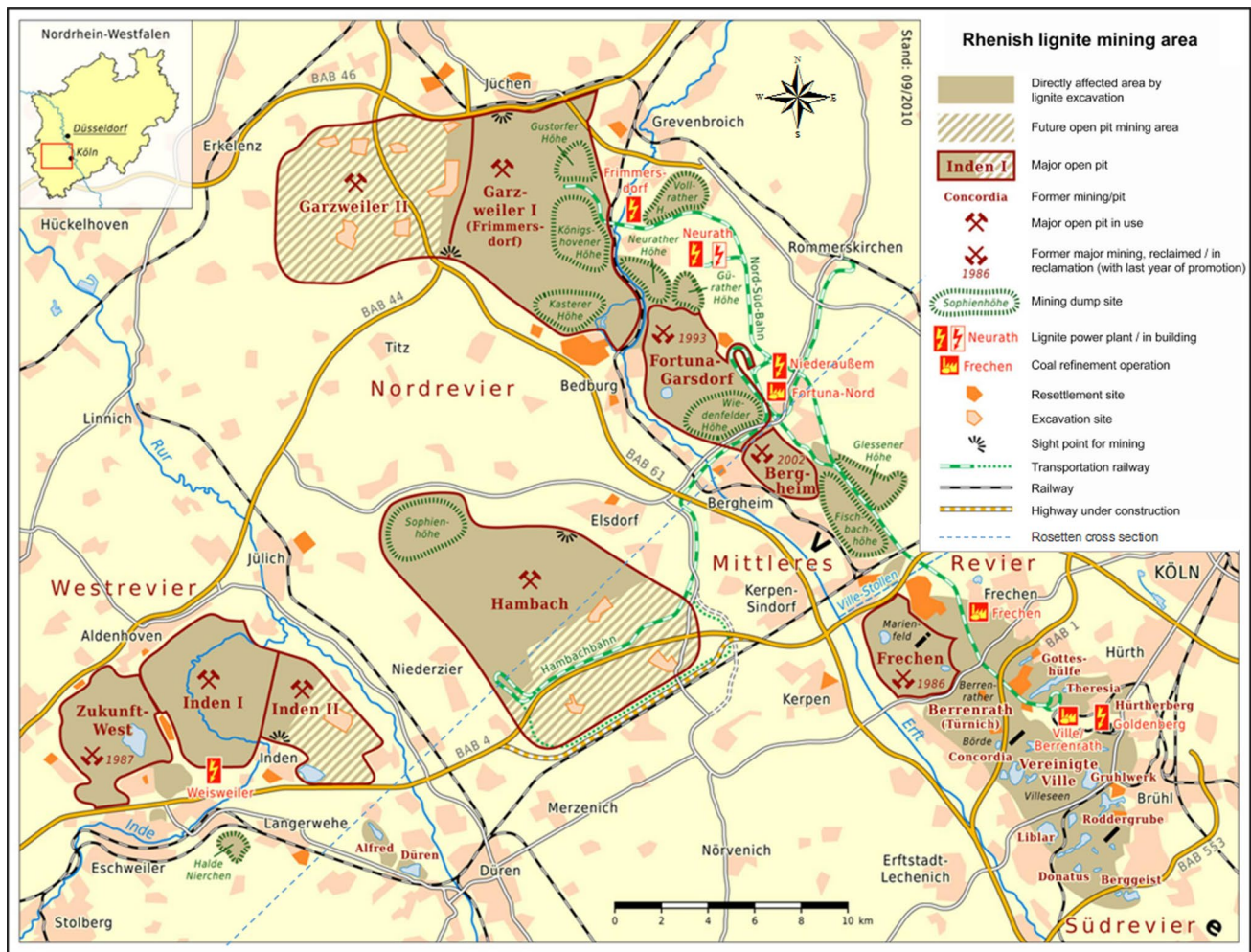
Fig. 1 Location of the Hambach mine in Germany (Thomas Roemer, OpenStreetMap data)

measured in the laboratory could not be adjusted to the actual measured deformation. Therefore, several indirect calculations needed to be carried out to determine the geotechnical parameters. Pre-evaluation of geotechnical parameters ensured the reliability of the indirect calculations.

The soil model (both clay and sand) used for numerical simulation consists of six fundamental parameters: density, Young's modulus (E), Poisson's ratio (v), friction angle (ϕ), cohesion (c) and dilation angle (ψ), which are required under the Mohr–Coulomb (M–C) criterion. A number of failure criteria have been proposed for the simulation of soil behavior; however, the M–C criterion is still widely applied when solving geotechnical engineering problems.

Dilation angle

It was not necessary to perform a sensitivity analysis for the dilation angle because the slope is a relatively unconfined object. For the numerical simulation of soil slopes,

the non-associated flow rule is usually adopted. Under the non-associated flow rule, the dilation angle is assigned to be zero for soils in the widely used numerical simulation platforms such as ABAQUS and FLAC3D.

Density

Regarding the density of the scanned slope material, Karcher (2003) has illustrated the relationship between density and material depth in the Lower Rhine area. The measured density of sand from a depth of 20–450 m is shown in Fig. 3a, while the density of clay in the region (between 2050 and 2400 kg/m^3) was also measured and is shown in Fig. 3b.

By regression analysis, the density of sand and clay at a specific depth T can be calculated via Eqs. (1) and (2), respectively:

$$\rho_{sand} = 2.0287 + 0.016845 \times \ln T + 0.001593 \times (\ln T)^2 - 0.000276 \times (\ln T)^3 \tag{1}$$

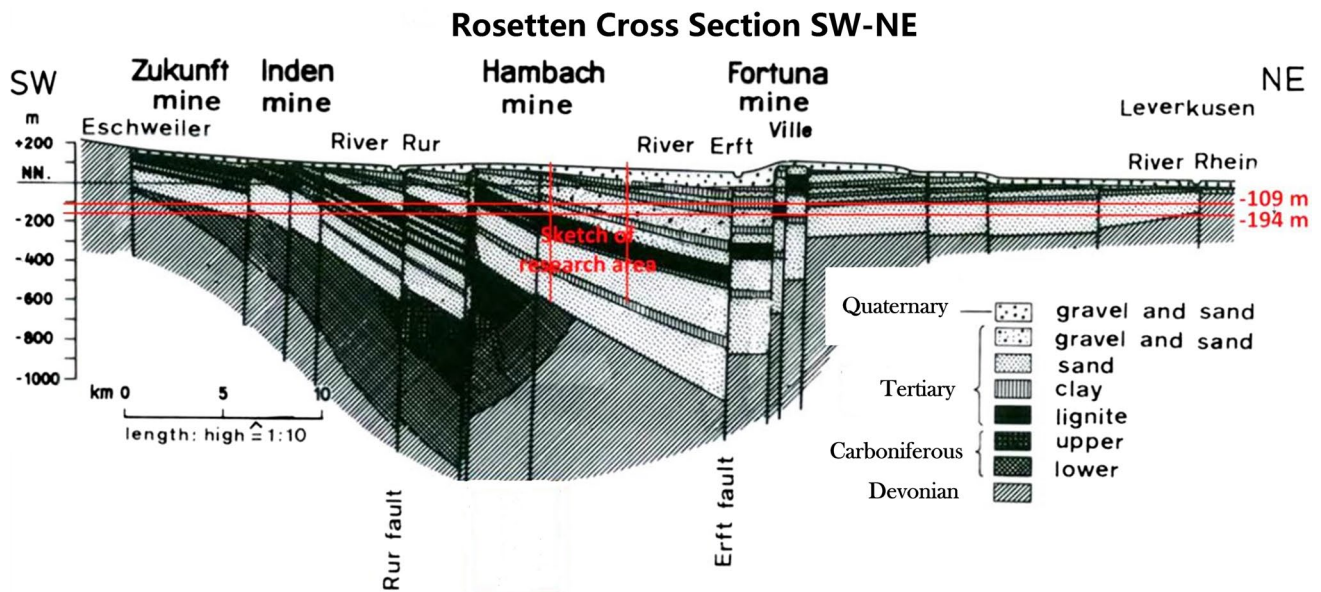## Rosetten Cross Section SW-NE

Fig. 2 Lithologic information for the Lower Rhine Basin along Rosetten cross section SW–NE (Schaefer et al. 2005, the Rosetten cross section is drawn in Fig. 1) with TLS scanned area highlighted by four perpendicular red lines

$$\rho_{clay} = 1.8380 + 0.1475 \times \ln T - 0.0308 \times (\ln T)^2 + 0.0031 \times (\ln T)^3 \tag{2}$$

Cohesion and friction angle

When the slope deformation is in an elastic phase, the impacts of shear strength parameters, i.e., cohesion c and friction angle ϕ, are approximately zero (Fig. 4). Figure 4 shows that the mechanical behavior of the model is in the elastic phase, when other parameters are fixed with maximum values. Therefore, with a decrease in either c or ϕ, the maximum deformation remained stable at about 0.08 m.

Young's modulus

The deformation of the scanned slope is highly dependent on the stiffness of the clay and sand. Therefore, it is important to determine the appropriate modulus of sand and clay for performing a precise slope stability analysis. Richmond and Briaud (2001) reviewed different modulus types that can be used for various geotechnical engineering applications. In the present study, the main reason for deformation was overburdened excavation. Thus, the unloading modulus E_u, which plays an important role in deformation behavior, needs to be precisely determined. E_u can be used in excavation analysis when dealing with deformation and heaving at the base of an excavation.

Sensitivity analysis for unloading modulus E_u was carried out and is shown in Fig. 5. Results show that the displacement was highly sensitive to the modulus. Thus,

deformation back analysis was adopted to determine the value of modulus. The modulus domain was defined as sand [10,200] and clay [10,200]. These modulus domains impacted the displacement power at a magnitude ranging from 6 to 28 cm. The displacement decreased with an increase in modulus. Given that the impact of modulus to displacement was linear in form, the correlation coefficient was still acceptable. It may illustrate a way in which parameters can be inverted using mechanical calculation.

In accordance with the German Institute for Standardization DIN 18196, the parametric domains of determination of the geotechnical parameters are listed in Table 1. Density was calculated by Eqs. (1) and (2). Poisson's ratio, friction angle and cohesion were not considered to be sensitive to deformation and were determined by the DIN 18196. Young's modulus was determined by deformation back analysis.

Methodology

Real 3D geological and geotechnical modeling

A higher-grade numerical model and more precise geotechnical parameters could produce more reliable analysis results. Thanks to rapid development of 3D geological modeling and geotechnical parameter prediction technologies, high-resolution 3D geological and geotechnical models are available for conversion into numerical simulation. A "real" 3D geological and geotechnical model can store soil

Fig. 3 Density of sand **a** and density of clay, **b** versus depth in the Lower Rhine area (Karcher 2003)
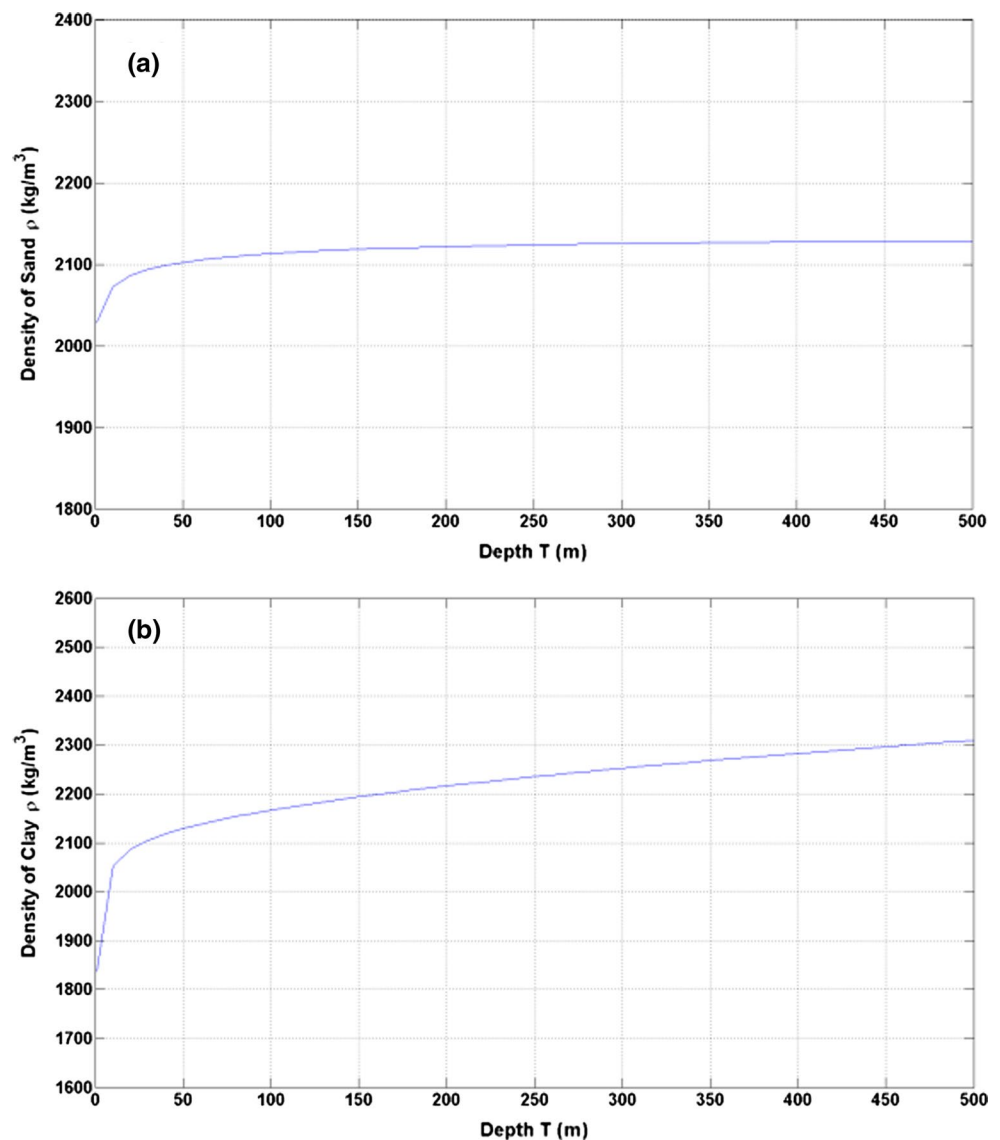
and rock characteristics at the actual position for further calculation.

A 3D geological and geotechnical model of a slope is normally comprised of the top surface of the slope, the boundary surface between two geological layers, the geotechnical parameters of each geological layer and the bottom surface. The top surface was established using a triangular irregular network (TIN) model of the elevation data acquired from LiDAR scanning. LiDAR technology was used to scan the slope and obtain high-resolution surface height data and the boundary of two soil layers. Then, for a simple slope model, the boundary surface between two geological layers was established by expanding the boundary lines identified in the LiDAR scans. LiDAR point cloud data were edited and processed using commercial software PolyWorks (www.innov metric.com). The paradigm GoCAD platform (www.pdgm.

com) was selected for the 3D geological modeling. In addition, GoCAD enables the convenient input of data exported from PolyWorks as a TXT file with *xyz* coordinates.

The second step was to construct the 3D geotechnical model. The 3D geological model of the study slope consisted of three border surfaces: the top surface, the border surface separating clay and sand and the bottom surface. Each block of clay and sand was meshed and interpolated in GoCAD with hexahedral elements. Each element was assigned with its own geotechnical parameters to form a 3D model that stores and provides detailed information for the object (Dong et al. 2015). In this study, geotechnical parameters (density, cohesion, friction angle, Young's modulus and Poisson's ratio) were assigned to the soil for numerical simulation and analysis.
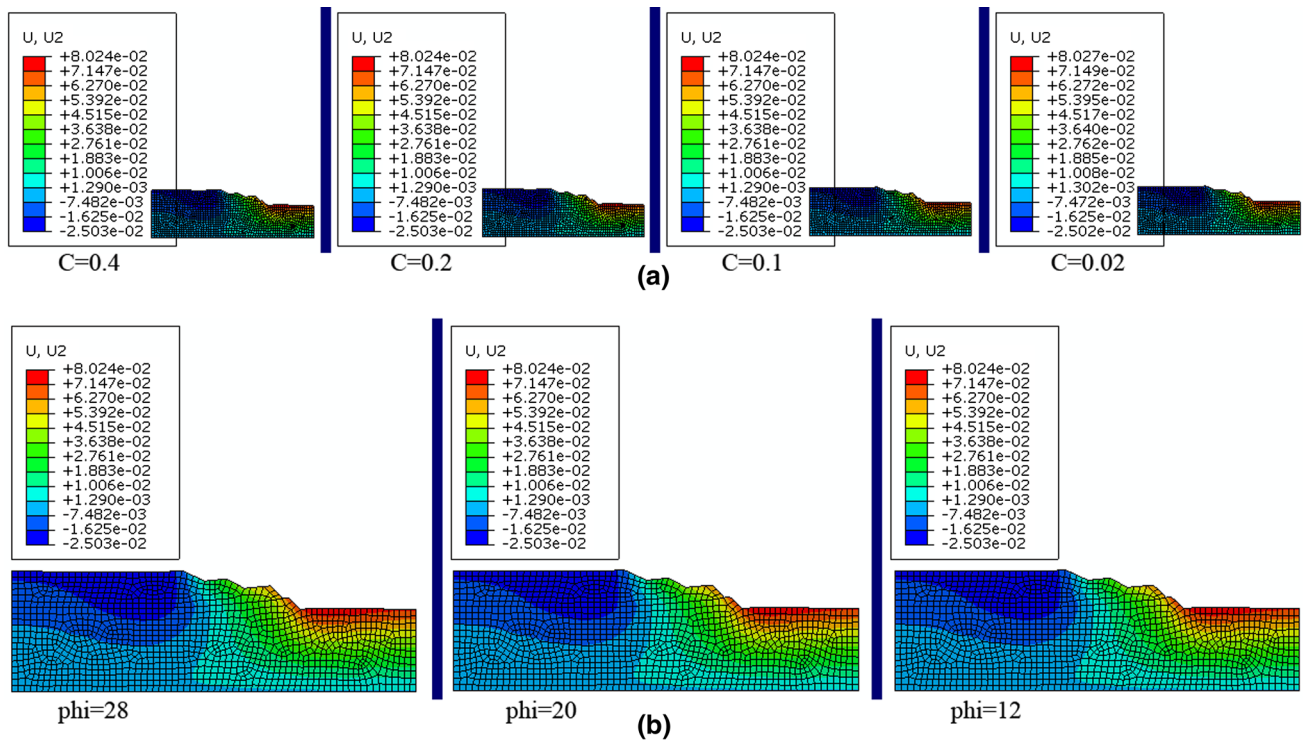
Fig. 4 Zero impacts of cohesion (part **a**) and friction angle (part **b**) to displacement. u2 represents vertical displacement. *C* represents cohesion *c* and phi represents friction angle ϕ
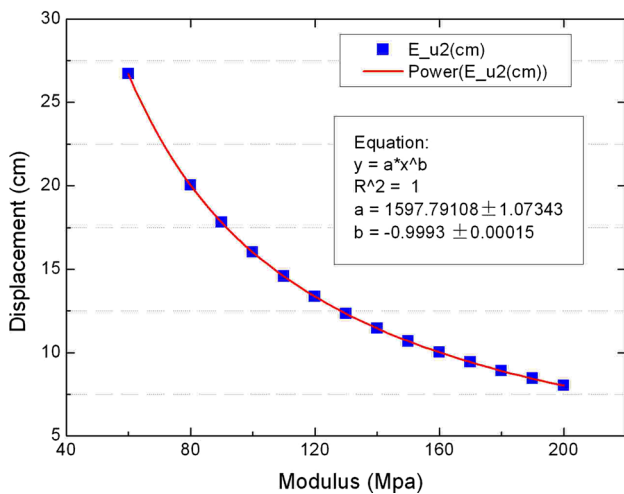

Fig. 5 Influence of unloading modulus on slope deformation

Table 1 Parametric domains for the determination of geotechnical parameters for the clay and sand

|	Clay	Sand
Density (kg/m^3)	2100–2300	2050–2150
Young's modulus (Mpa)	10–200	10–200
Poisson's ratio	0.4	0.3
Friction angle (°)	10–25	30–40
Cohesion value (Mpa)	0.01–0.4	0.00001–0.01
Dilation angle (g°)	–	–

Numerical model conversion

A prior paper was published that described how to convert the 3D geotechnical model produced by GoCAD into a numerical model in ABAQUS (Hu et al. 2012). Following this method, the geotechnical model was transformed into a numerical model, which is shown in Fig. 6. In the present study, the geometrical model was extracted using two planes that were perpendicular to the strike of the slope surface and cut across the scanned model. The dimension of the extracted numerical model was determined by the position of the two cutting planes. As shown in Fig. 6, the height differential from the fifth to the sixth levels was 54.86 m. The thickness of the sand layer was 26.14 m and the clay layer was 48.36 m. The bottom length of the model was 345.25 m. The top length was 126.7 m, and the width of the model was 73.7 m. The numerical model was comprised of 246,164 hexahedral elements.

Fig. 6 3D numerical model for slope stability analysis
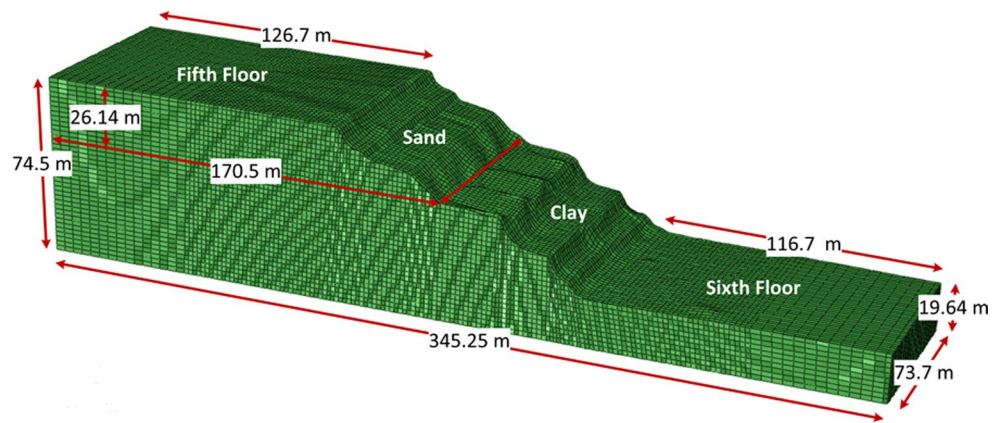
Back analysis of geotechnical parameters

BPNN methodology

A back-propagation neural network (BPNN) can be described as a multi-layer, dynamic system optimization neural network. It is a supervised trial-and-error learning procedure that identifies the correlation between input and output parameters. Basically, the implementation of a BPNN is divided into two phases: forward (propagation) and backward (error minimizing). A BPNN system consists of three kinds of layers: the input layer, certain hidden layers and the output layer. Each layer consists of many neurons. In the first phase, the neurons of the input layer receive input data without any transformation. Then, the input layer sends data to the hidden layers via weight transformation. Finally, the output layer is activated by the propagation output. The difference between the output and the observed data should be calculated to improve the reliability of the network. In the second phase, the difference is applied to minimize the error by updating the weight. The two phases will be repeated until the difference reaches an acceptable value. More complex systems typically have more hidden layers with greater numbers of neurons. The BPNN workflow for the determination of geotechnical parameters is shown in Fig. 7 and can be described as follows:

(1) Sample preparation: orthogonal design and normalization of geotechnical parameters within the parametric domain, forward FEM calculation of the deformation and creation of the map from parameters to deformation (① and ② in Fig. 7);

(2) Configuration of neural networks: set up the number of hidden layers and hidden nodes (the box of BPNN in Fig. 7);

(3) BPNN training and testing: calculated displacement in step (1) as the input, corresponding geotechnical parameters as the target, training of the network between the input and output and testing of the network (③ in Fig. 7);

(4) Determination of targeted parameters: monitored displacement as the input, use the trained network to obtain the geotechnical parameters (outputs), then estimate the quality of outputs (④ to ⑦ in Fig. 7);

(5) Iteration: if the estimated correlation between displacements calculated by geotechnical parameters and monitored displacements is poor, go to step (3) to promote the network.

Implementation of BPNN

In order to speed up the process, the slope shown in Fig. 6 was divided into three groups, Group 1, Group 2 and Group 3, and deformation was measured for each group independently. In each group, a feature point was selected using the feature degree method. The deformation of each group was represented by the measured displacement of the feature point.

Input parameters were displacement values from the three groups, d_1, d_2 and d_3. Output parameters were E_u of sand and E_u of clay. The hidden layer was set up to one layer. A sigmoidal transfer function was selected to connect each layer. The training function *trainglm* was used to update the weight and bias values according to Levenberg–Marquardt optimization (Marquardt 1963; Levenberg 1944).

During sample preparation, two geotechnical parameters (Young's modulus for sand and clay) and seven arrays were selected for orthogonal design, which is known as the L49 array structure (Table 2). As discussed in Sect. 2.3, shear strength parameters c and ϕ, Poisson's value and density were determined based on Table 1.

To create the map of geotechnical parameters to displacement, forward FEM calculation was carried out. The 49 samples used as inputs into the FEM program produced 49 deformed models. For each model, the deformation of three points that correspond to the three slope groups was obtained and is shown in Table 2.

Fig. 7 BPNN workflow
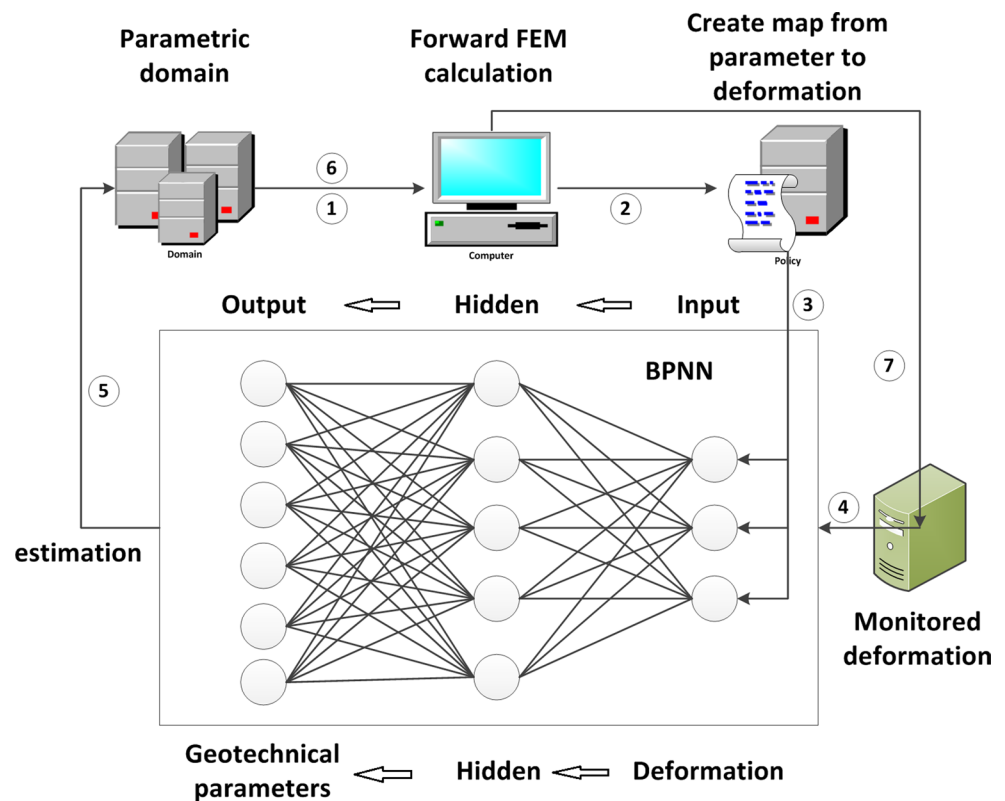
The samples were not directly used for BPNN analysis. They first needed to be normalized to a value domain, i.e., [− 1,1].

Null value and singular value in the prepared samples (Table 2) were removed from further calculation. Then, 36 samples remained for BPNN. Of the 36 samples, 32 random samples were reserved for training, and the remaining four were used for testing. Figure 8 shows the correlation between training sample targets and outputs, with a coefficient of 0.98794. Figure 9 shows the correlation coefficient of 0.94191 between testing sample targets and outputs. These results showed that the learning procedure was qualified to predict parameter E_u.

Table 3 shows the geotechnical parameters that were determined for slope stability analysis. Density was calculated based on Eqs. (1) and (2), and the densities of sand and clay were 2125 and 2268, respectively. E_u values for sand and clay were obtained based on BPNN and were 80 and 96 Mpa, respectively. Empirical values of 0.3 and 0.4 are selected as the respective Poisson's ratios for sand and clay. The ratio for clay (0.4) was relatively high; however, this corresponded to the field conditions at the study site.

Verification of determined geotechnical parameters

To verify the reliability of the obtained E_u values and selected geotechnical parameters, the calculated deformation was compared with the observed deformation. The comparison results are shown in Table 4. The maximum discrepancy between the calculated and observed deformation values was 3.33%, which demonstrates that the determined geotechnical parameters were adequate for further numerical simulation.

Automatic strength reduction finite-element method

The shear strength reduction technique (SRT) was adopted by Griffiths to obtain the safety factor of a slope (Griffiths and Lane 1999), which makes results calculated by the finite-element method relative to those calculated by LEMs. SRT has been applied to slope stability analysis for decades. With the development of computer technology, especially nonlinear elasto-plasticity finite-element method (FEM) computing technology for geotechnical materials, SRT is increasingly being applied in geotechnical engineering. In addition, scholars have been dedicated to research on merging the SRT with FEM for slope stability analysis (Huang and Jia 2009). In the implementation of the strength reduction finite-element method, the traditional solution is to modify the strength parameters in the input file or in a computer-aided engineering (CAE) interface based on an increase in reduction factors from trial calculation, and the process is manual and time-consuming. In addition to this limitation, it is difficult to implement the time series analysis.

Table 2 Sample preparation based on L49 array structure

| L49 structure		Sand	Clay	Displacement		
v_1	v_2	E_u (Mpa)	E_u (Mpa)	d_1 (cm)	d_2 (cm)	d_3 (cm)
1	1	190	190	5.25	6.22	6.78
1	2	190	160	6.24	7.39	8.05
1	3	190	130	7.68	9.10	9.91
1	4	190	100	/	/	/
1	5	190	70	/	/	/
1	6	190	40	/	/	/
1	7	190	10	/	/	/
2	1	160	190	5.26	6.23	6.78
2	2	160	160	6.24	7.39	8.05
2	3	160	130	7.68	9.09	9.91
2	4	160	100	9.99	11.83	12.89
2	5	160	70	14.30	16.91	18.43
2	6	160	40	/	/	/
2	7	160	10	/	/	/
3	1	130	190	5.28	6.24	6.80
3	2	130	160	6.25	7.40	8.06
3	3	130	130	7.68	9.09	9.91
3	4	130	100	9.98	11.82	12.89
3	5	130	70	14.28	16.90	18.42
3	6	130	40	/	/	/
3	7	130	10	/	/	/
4	1	100	190	5.30	6.26	6.81
4	2	100	160	6.28	7.42	8.08
4	3	100	130	7.70	9.11	9.92
4	4	100	100	9.98	11.82	12.88
4	5	100	70	14.27	16.89	18.41
4	6	100	40	/	/	/
4	7	100	10	/	/	/
5	1	70	190	5.34	6.29	6.84
5	2	70	160	6.32	7.45	8.11
5	3	70	130	7.75	9.15	9.96
5	4	70	100	10.02	11.85	12.91
5	5	70	70	14.26	16.89	18.41
5	6	70	40	24.99	29.57	32.23
5	7	70	10	/	/	/
6	1	40	190	5.38	6.33	6.87
6	2	40	160	6.38	7.50	8.15
6	3	40	130	7.83	9.21	10.01
6	4	40	100	10.13	11.94	12.98
6	5	40	70	14.37	16.98	18.48
6	6	40	40	24.95	29.55	32.21
6	7	40	10	/	/	/
7	1	10	190	5.43	6.37	6.91
7	2	10	160	6.45	7.56	8.20
7	3	10	130	7.93	9.30	10.08
7	4	10	100	10.29	12.08	13.10
7	5	10	70	14.67	17.22	18.69
7	6	10	40	25.51	30.00	32.59
7	7	10	10	99.80	118.20	128.85
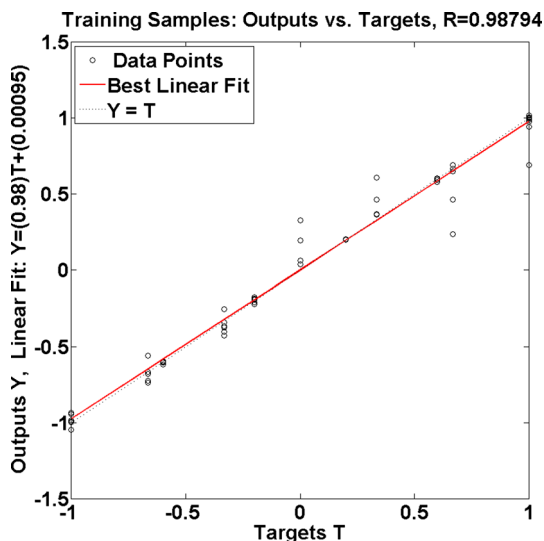
Fig. 8 Correlation between training sample targets and outputs
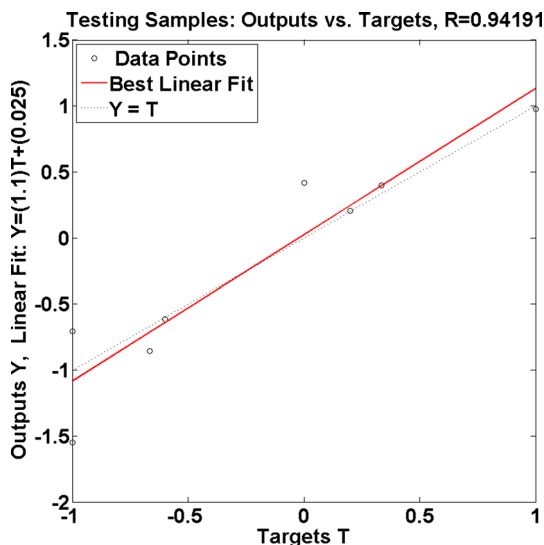

Fig. 9 Correlation between testing sample targets and outputs

Table 3 Determined geotechnical parameters for the scanned slope

	Clay	Sand
Density (kg/m³)	2268	2125
Young's modulus (Mpa)	96	80
Poisson's ratio	0.4	0.3
Friction angle (°)	25	35
Cohesion value (Pa)	60000	10

In order to improve computational efficiency and reveal the relationship between the safety factor and the time step variable, a field variable (FV)-based technique was proposed

Table 4 Comparison of calculated and observed deformations

Example	$t1$	$t2$	$t2$
Observed deformation (cm)	10.83	12.33	13.52
Calculated deformation (cm)	10.81	12.74	13.97
Discrepancy (%)	− 0.18	3.33	3.33

in the current study for automatic strength reduction calculation. The cohesion and internal friction angles were reduced with the automatic increase in the time step variable t during the implementation of FEM in ABAQUS, and the FOS was determined in a complete analysis step.

Equation 3 describes the fundamentals of the strength reduction technique.

$$\begin{cases} c'_{\mathrm{f}} = \dfrac{c'}{F_{\mathrm{s}}} \\ \phi'_{\mathrm{f}} = \tan^{-1} \dfrac{\tan \phi'}{F_{\mathrm{s}}} \\ \psi'_{\mathrm{f}} = \tan^{-1} \dfrac{\tan \psi'}{F_{\mathrm{s}}} \end{cases} \tag{3}$$

where c'_{f}, ϕ'_{f} and ψ'_{f} are effective cohesion, internal friction angle and dilation angle at the critical state of slope failure, respectively. At the same time, F_{s}, which divides the original c', ϕ' and ψ', is considered to be the factor of safety (FOS). For the purpose of simplification, the dilation angle is often defined as zero, i.e., non-associated flow rule.

The widely used Mohr–Coulomb (M–C) criterion was adopted as the yield criterion (Fig. 10).

FV-based strength reduction

For simplification, the selection of the linear function creates the relationship between FV f and time step variable t:

$$f(t) = a - bt \tag{4}$$

where f is the field variable, t is the time step variable, and a and b are adjustable parameters.

The universal strength reduction can be described in Eq. (5):

$$\begin{cases} c' = fc'_{\mathrm{ini}} \\ \tan \phi' = f \tan \phi'_{\mathrm{ini}} \end{cases} \tag{5}$$

where c'_{ini} and ϕ'_{ini} are the initial effective cohesion and the initial effective internal friction angle, respectively; c' and ϕ' are the cohesion and friction angles corresponding to FV.

Therefore, the relationship between shear strength parameters and the time step variable can be described by Eq. (6):

$$\begin{cases} c' = (a - bt)c'_{\mathrm{ini}} \\ \tan \phi' = (a - bt) \tan \phi'_{\mathrm{ini}} \end{cases} \tag{6}$$

Fig. 10 Mohr–Coulomb failure criterion
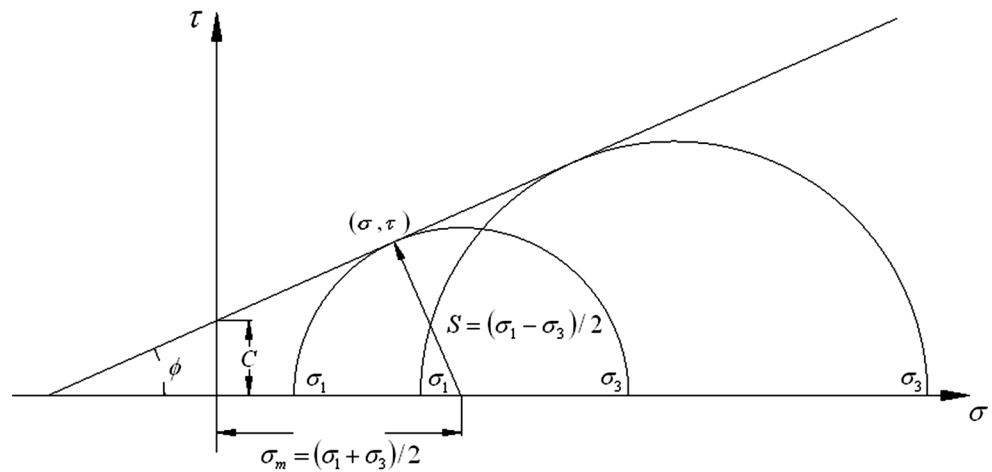
Finally, the relationship of FOS F_s and the time step variable can be written as Eq. [7]:

$$F_s = \frac{1}{a - bt} \qquad (7)$$

Implementation of FV-based strength reduction

In the FV-based method, the two adjustable parameters a and b need to be clarified. When $F_s > 0$ and the time step variable $0 \leq t \leq 1$, both a and b are positive. It is required that $\frac{a}{b} > 1$ and $b \neq 0$. The determination of a would influence the minimum potential FOS value, while the magnitude of a-b affects the maximum potential FOS value. Figure 11 illustrates the flowchart of the FV-based strength reduction method.

The calculation of displacement forms the basis for slope stability analysis. If the calculated displacement represents a leap prior to the divergence calculation, that leap point represents the FOS; if not, the divergent point represents the FOS. In addition, a more objective approach simultaneously takes the state of equivalent plastic strain into account for determining the FOS. Regarding the FV-based strength reduction technique, the starting point represents an FOS of 1, and the end point represents an FOS of 2. Whichever point (leap or divergent) is located between analysis increments two and three will indicate the FOS.

Results and discussion

In order to observe the FOS-dependent change of displacement and plastic strain, two groups of observation points were selected from the slope surface and plastic strain zone and defined as "GS" and "GZ." GS consisted of nodes 8, 7, 6, 5, 4, 3 and 17, which were located on
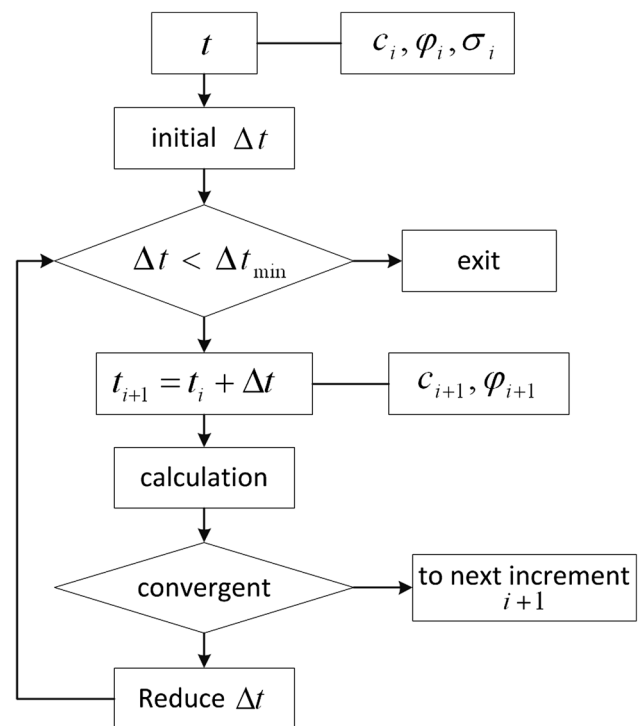

Fig. 11 Flowchart of the FV-based strength reduction method

the slope surface from top to bottom. GZ was comprised of nodes 3, 75, 74, 576, 856, 4060 and 616, which were located on the plastic strain zone. The positions of the GS and GZ nodes were labeled in a simplified 2D slope cross section, which is shown in Fig. 12.

Results

The horizontal displacement, vertical displacement, total displacement and plastic strain versus FOS for both GS and GZ are shown in Figs. 13, 14, 15, 16, 17, 18, 19 and 20. In
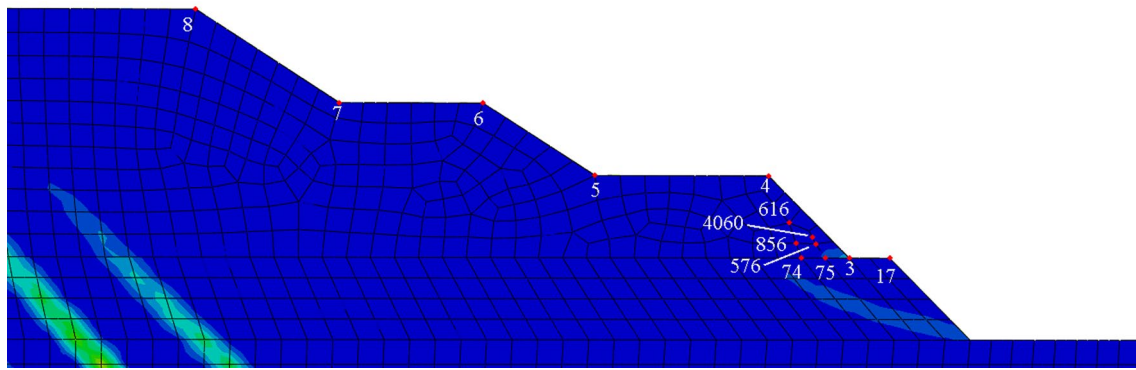
Fig. 12 Locations of the GS and GZ nodes. GS: group of nodes located along the slope surface. GZ: group of nodes located at the plastic strain zone
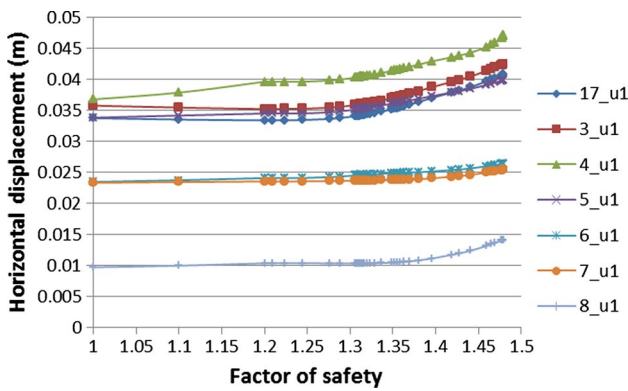

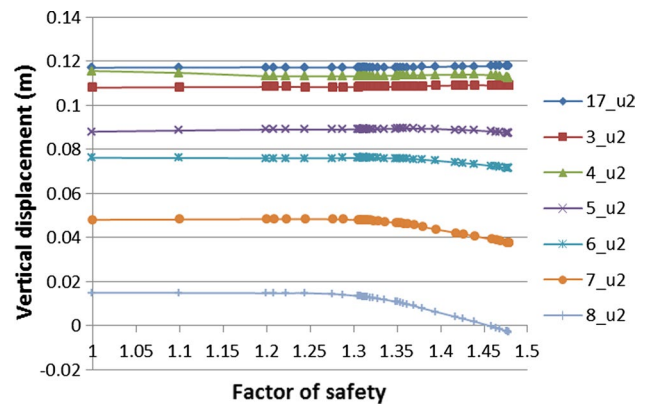**Fig. 13** Horizontal displacement versus FOS of the observed surface nodes

Fig. 14 Vertical displacement versus FOS of the observed surface nodes

Figs. 13, 14, 15, 16, 17, 18, 19 and 20, *um* represents total displacement, *u*1 represents horizontal displacement, and *u*2 represents vertical displacement.

Figure 13 shows the horizontal displacement versus FOS of all GS nodes. Nodes 8, 7 and 6, which were located relatively far away from the plastic strain zone, had relatively small horizontal displacements. Nodes 5, 4, 3 and 17, which were located near the plastic strain zone, had relatively larger horizontal displacements, particularly nodes 5, 4 and 3. All displacement leap points for the GS nodes were located at an FOS of 1.3.

Figure 14 shows the vertical displacement versus FOS of all GS nodes. The vertical displacements for nodes 8, 7, 6 and 5 remained stable until FOS reached 1.3, at which point they decreased linearly until computation ended at an FOS of 1.48. In contrast, the vertical displacements of nodes 4, 3 and 17 remained stable from the beginning of the strength reduction to the end.

Figure 15 shows the total displacement versus FOS of all GS nodes. The higher nodes had smaller displacement
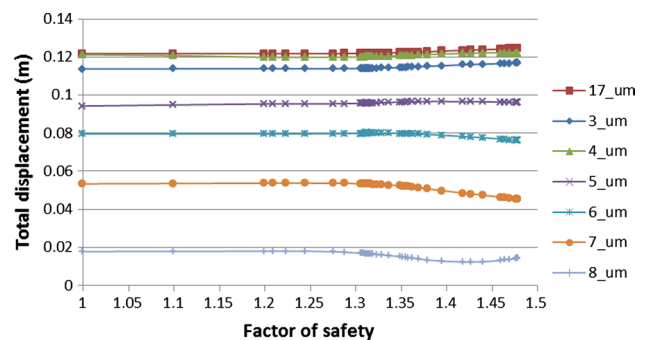

Fig. 15 Total displacement versus FOS of the observed surface nodes

values. Leap points at FOS of 1.3 could be identified based on the curves of nodes 5, 6, 7 and 8.

The horizontal displacement versus FOS for all GZ nodes is shown in Fig. 16. The horizontal displacements of nodes 4060, 576, 616 and 856 increased as strength
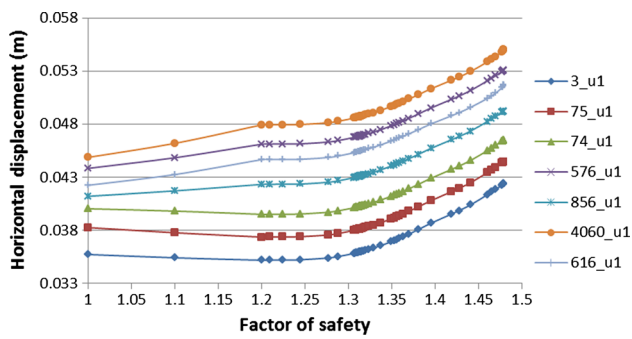
Fig. 16 Horizontal displacement versus FOS of the observed surface nodes in the plastic strain zone
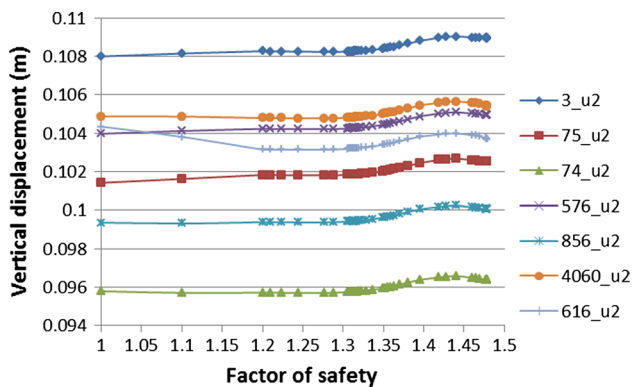

Fig. 19 Plastic strain versus FOS of the observed surface nodes

Fig. 17 Vertical displacement versus FOS of the observed nodes in the plastic strain zone

Fig. 20 Plastic strain versus FOS of the observed nodes in the plastic strain zone

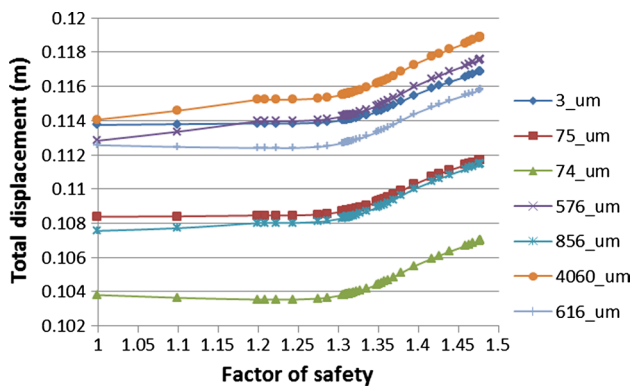**Fig. 18** Total displacement versus FOS of the observed nodes in the plastic strain zone

was reduced and stopped at an FOS of 1.2. They remained stable until FOS reached 1.3, at which point they increased linearly until FOS reached 1.48. On the other hand, horizontal displacement values for nodes 74, 75 and 3, which were located on the same level of the model, remained stable until FOS reached 1.3, and then linearly increased
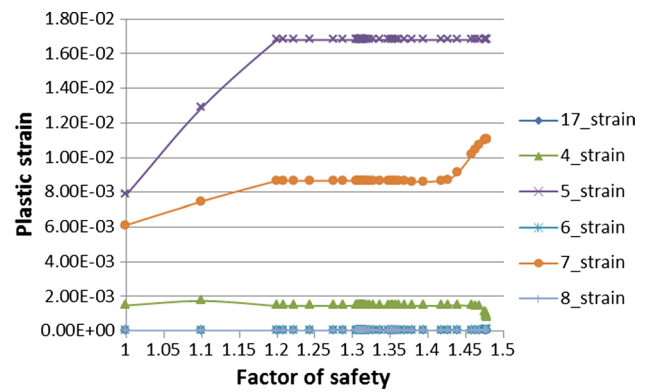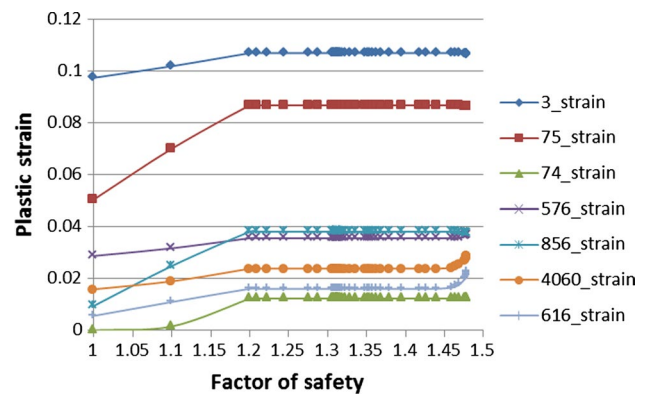
until FOS reached 1.48. All the curves had leap points at an FOS of 1.3.

The vertical displacement versus FOS for all GZ nodes is shown in Fig. 17. Node 3 had the largest vertical displacement from the beginning of the strength reduction to the end, and its leap occurred at an FOS of 1.34. Node 74, which was located relatively far away from the potential slip zone, had the smallest vertical displacement. All curves had leap points at an FOS of 1.34 except for node 616.

The total displacement versus FOS for all GZ nodes is shown in Fig. 18. The total displacement of nodes 4060, 576 and 856 increased linearly until FOS reached 1.2, then remained stable until FOS reached 1.3 and continued to increase again until FOS reached 1.48. On the other hand, total displacement values for nodes 3, 616, 75 and 74 remained stable until FOS reached 1.3, at which point they increased to an FOS value of 1.48.

Furthermore, the plastic strain of the observed nodes was another way to determine the FOS and reveal the potential slip zones. Figure 19 shows the plastic strain versus FOS of all GS nodes. Only nodes 5 and 7 had small plastic strain levels that could be ignored, while the plastic strain values

Fig. 21 Time stamps along the D-AI curve for nodes 4 and 17. u2 represents vertical displacement
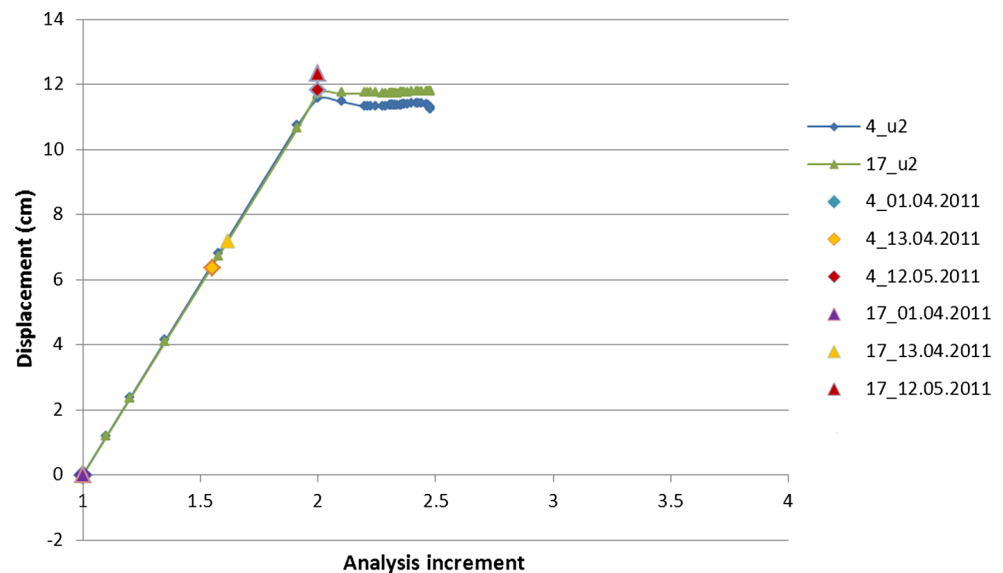
for nodes 8, 6, 4 and 17 were approximately zero. This is because all GS nodes were located on the slope surface. Nodes 5 and 7 were the vertices of the concave, while the other nodes were the vertices of convex. The end points of all curves had FOS values of 1.48. Figure 20 shows the plastic strain versus FOS for all GZ nodes. Node 3 had the largest plastic strain for all selected GZ nodes and was followed by node 75. This demonstrates that the toe of the potential slip zone might be node 3. All curves had leap points at FOS of 1.2 and ceased at FOS of 1.48.

Figures 13, 14, 15, 16, 17, 18, 19 and 20 show that there were recognizable but negligible leap points at FOS of 1.2 and 1.3. Therefore, the subordinate failure criteria, i.e., the divergent point basis, were adopted in the present study. Finally, the FOS was 1.48.

Time effect discussions

In order to take the time effect into account for the FEM simulation, the time stamps from different scanning campaigns were marked along the displacement curve, versus the analysis increment (D-AI curve). The first scan campaign on April 1, 2011, was assumed as the starting of unloading process on the D-AI curve. This assumption meant that the displacement after unloading (excavation) and prior to the first scan campaign was 0. Then, the third scan campaign on May 12, 2011, was assumed as the starting of the SRT process on the D-AI curve, i.e., an analysis increment of 2. The measured vertical displacements from the second scan were 0.0636, 0.072 and 0.0882 m for Groups 1, 2 and 3, respectively. Groups 1 and 2 were approximately represented by GS nodes 4 and 17. Therefore, the D-AI curves for those nodes were selected for the time stamps, which are shown in Fig. 21.

Due to the influence of ongoing mining operations and weather conditions, the last scanning campaign was performed on June 20, 2011. There were 39 days between the third and final scanning campaigns. The long interval made it difficult to determine which process the third scan campaign represented on the D-AI curve, i.e., whether it was a unloading process or a SRT process. It also made the last scan campaign useless in the discussion about the effect of time. In Fig. 21, the time stamps from the second campaign for two nodes are situated apart on the D-AI curve, identified by a yellow triangle (node 17) and a yellow diamond (node 4), because the x-axis was the analysis increment but not the actual time. The four time stamps roughly formed a parabola, in which the third time stamp location was considerably important. The discussion of the effect of time is useful for determining the actual FOS value and predicting displacement. However, the above two assumptions generated uncertainty, which could be resolved in the future by increasing the number of scanning campaigns.

Conclusions

The strength reduction finite-element method has been widely adopted for slope stability analysis. However, challenges such as adequate data acquisition, precise numerical models and adaptable methodologies have made reliable analysis results difficult to obtain. This study proposed a combined methodology to solve these challenges associated with slope stability analysis. First, LiDAR technology was used to capture the high-resolution geometry of the slope. Then, 3D geological and geotechnical modeling along with data converting technology were adopted to create a

high-quality numerical model for simulation. Third, a field variable-based, automatic strength reduction technique was combined with the finite-element method to analyze complex geotechnical problems. A time series was considered in the methodology to improve the reliability of the determined FOS. The deepest open pit mine in Hambach, Germany, was used as a case study to demonstrate the effectiveness and applicability of the adopted methodology, which can also be applied in other slope settings.

References

Arikan F, Yoleri F, Sezer S, Caglan D, Biliyul B (2010) Geotechnical assessments of the stability of slopes at the Cakmakkaya and Damar open pit mines (Turkey): a case study. Environ Earth Sci 61(4):741–755. https://doi.org/10.1007/s12665-009-0388-7

Bishop A (1955) The use of the sliding circle in the stability analysis of slopes. Geotechnique 5:7–17

Dong M, Neukum C, Hu H, Azzam R (2015) Real 3D geotechnical modeling in engineering geology: a case study from the inner city of Aachen, Germany. Bull Eng Geol Enviorn 74:281–300. https://doi.org/10.1007/s10064-01400640-6

Glastonbury J, Fell R (2002) A decision analysis framework for assessing post-failure velocity of natural rock slopes. University of New South Wales, Sydney

Gonte E, Donato A, Troncone A (2013) A finite element approach for the analysis of active slow-moving landslides. Landslides 11(4):723–731. https://doi.org/10.1007/s10346-013-0446-9

Griffiths DV, Lane PA (1999) Slope stability analysis by finite elements. Geotechnique 49(3):387–403

Hu H, Fernandez-Steeger TM, Dong M, Azzam R (2012) Numerical modeling of LiDAR-based geological model for landslide analysis. Autom Constr 24:184–193. https://doi.org/10.1016/j.autcon.2012.03.001

Huang M, Jia CQ (2009) Strength reduction FEM in stability analysis of soil slopes subjected to transient unsaturated seepage. Comput Geotech 36:93–101

Huang MS, Fan XP, Wang HR (2017) Three-dimensional upper bound stability analysis of slopes with weak interlayer based on rotational-translational mechanism. Eng Geol 223:82–91. https://doi.org/10.1016/j.enggeo.2017.04.017

Jiang SH, Li DQ, Zhang LM, Zhou CB (2014) Slope reliability analysis considering spatially variable shear strength parameters using a non-intrusive stochastic finite element method. Eng Geol 168(1):120–128. https://doi.org/10.1016/j.enggeo.2013.11.006

Jiang Q, Qi Z, Wei W, Zhou C (2015) Stability assessment of a high rock slope by strength reduction finite element method. Bull Eng Geol Enviorn 74:1153–1162. https://doi.org/10.1007/s10064-01400689-1

Karcher C (2003) Tagebaubedingte Deformationen im Lockergestein. Ph.d. dissertation, Karlsruhe Institute of Technology

Kaya Y, Topal T (2015) Evaluation of rock slope stability for a touristic coastal area near Kusadasi, Aydin (Turkey). Environ Earth Sci 74(5):4187–4199. https://doi.org/10.1007/s12665-015-4473-9

Kelesoglu MK (2016) The evaluation of three-dimensional effects on slope stability by the strength reduction method. KSCE J Civ Eng 20(1):229–242. https://doi.org/10.1007/s12205-015-0686-4

Levenberg K (1944) A method for the solution of certain problems in Least Squares. Q Appl Math 2:164–168

Lin H, Chen JY (2017) Back analysis method of homogeneous slope at critical state. KSCE J Civ Eng 21(3):670–675. https://doi.org/10.1007/s12205-016-0400-1

MacLaughlin MM, Doolin DM (2006) Review of validation of the discontinuous deformation analysis (DDA) method. Int J Numer Anal Methods Geomech 30(4):271–305. https://doi.org/10.1002/nag.427

Marquardt D (1963) An algorithm for least-squares estimation of non-linear parameters. SIAM J Appl Math 11:431–441

Nian TK, Huang RQ, Wan SS, Chen GQ (2012) Three-dimensional strength-reduction finite element analysis of slopes: geometric effects. Can Geotech J 49(5):574–588. https://doi.org/10.1139/t2012-014

Ozbay A, Gabalar AF (2015) FEM and LEM stability analyses of the fatal landslides at Gollolar open-cast lignite mine in Elbistan, Turkey. Landslides 12(1):155–163. https://doi.org/10.1007/s10346-014-0537-2

Richmond BC, Briaud JL (2001) Introduction to soil moduli. Geotech News 19(2):54–58

Schaefer A, Utescher T, Klett M, Valdivia-Manchego M (2005) The Cenozoic Lower Rhine Basin rifting, sedimentation, and cyclic stratigraphy. Int J Earth Sci 94:621–639

Scholtes L, Donze FV (2012) Modelling progressive failure in fractured rock masses using a 3D discrete element method. Int J Rock Mech Min Sci 52:18–30. https://doi.org/10.1016/j.ijrmms.2012.02.009

Sjoeberg J (2000) Slope stability in surface mining, Kap. Chapter 5: a slope height versus slope angle database, 47–57. Society for Mining Metallurgy and Exploration, Inc

Zhou XP, Cheng H (2013) Analysis of stability of three-dimensional slopes using the rigorous limit equilibrium method. Eng Geol 160:21–33. https://doi.org/10.1016/j.enggeo.2013.03.027